Journal of Nuclear Materials 402 (2010) 102–107

Contents lists available at ScienceDirect

Journal of Nuclear Materials

journal homepage: www.elsevier.com/locate/jnucmat

Experimental re-determination and thermodynamic assessment of the erbium–zirconium system

J. Jourdan [a,b], C. Toffolon-Masclet [a], J.-M. Joubert [b,*]

[a] CEA, DEN (Nuclear Energy Division), DMN/SRMA/LA2M, F-91191 Gif-Sur-Yvette, France
[b] Chimie Métallurgique des Terres Rares, Institut de Chimie et des Matériaux Paris-Est, CNRS, Université Paris-Est, 2-8 rue H. Dunant, 94320 Thiais, France

ARTICLE INFO

Article history:
Received 8 February 2010
Accepted 4 May 2010

ABSTRACT

The erbium–zirconium (Er–Zr) system has been completely reinvestigated experimentally. Particular attention was paid to the high purity of the raw materials, to the absence of oxygen contamination and to the control of the high vapor pressure of erbium. Several experimental techniques have been used to measure the solubility limits at different temperatures, the invariant points and the solidus and liquidus temperatures which were generally found to disagree with what was reported in the literature. As a result, the phase diagram presently obtained differs significantly from the accepted one and we propose a complete revision of the system. A thermodynamic assessment using the Calphad approach has been conducted. A set of parameters has been obtained allowing to describe well the experimental measurements.

1. Introduction

This work has been achieved in the framework of the development of innovating concepts for fuel cladding in pressurized water nuclear reactors. This concept implies the insertion of an internal erbium–zirconium layer in the zirconium fuel cladding [1]. Erbium is used as a burnable poison able to compensate the initial reactivity reserve in nuclear Light Water Reactors (LWR). Due to its lower absorption cross section compared to gadolinium which is presently used, it is particularly well adapted to achieve very high burnup in LWR. As a consequence, knowledge of the erbium–zirconium phase diagram is of primary importance to provide informations on the metallurgical synthesis of the insertion layer and to understand the interaction between the different layers. We present here a complete experimental re-determination of the phase diagram and, in a second part, a thermodynamic assessment using the Calphad method.

2. Literature survey

Only a few investigations have been devoted to the study of the erbium–zirconium system. It was investigated by Armantrout [2], Love [3] and Copeland and Kato [4]. Armantrout [2] measured the solubility limit of erbium in zirconium at 1000 °C. Love [3] measured the erbium solvus using X-ray data. He also investigated the solidus and liquidus temperatures and recorded differential thermal analysis (DTA) signals for several Er–Zr alloys. Copeland and Kato [4] studied the (α_{Zr}) to (β_{Zr}) transformation. They obtained three phases in equilibrium in several annealed alloys which is an obvious indication that the alloys had not reached equilibrium or that impurities were present in a significant amount. They report the corresponding peritectoid temperature and also the eutectic temperature.

All the available data have been compiled by Alcock et al. who have drawn a phase diagram [5] which is still the reference diagram in compilations [6,7]. This diagram is shown in Fig. 1 together with the various experimental data. The two invariant temperatures are from [4]. Given the small amount of data, the fact that some of them are contradictory or are obviously non-equilibrium data, this diagram should be considered as mainly speculative. No new experimental data has been made available since then and no new evaluation of the system has been proposed. No thermodynamic data is available either.

3. Experimental determination of the phase diagram

3.1. Experimental techniques

As starting materials, we selected pure de-hafnied zirconium metal (99.97%) obtained using the van Arkel process and pure distilled erbium metal (99.95%, China Rare Metals). Samples of 1–2 g were prepared with precaution in order to avoid oxygen contamination. Erbium was stored in a glove-box under purified argon atmosphere. The surface oxide of each metal was removed by mechanical abrasion just prior the melting. Adjusted amounts of metals pieces were then melted in an arc-furnace under argon atmosphere (U grade, 800 mbar) purified by melting a zirconium getter. The samples were melted four times and turned upside down between each melting to ensure complete melting and good

---

* Corresponding author. Tel.: +33 1 49 78 12 11; fax: +33 1 49 78 12 03.
E-mail address: jean-marc.joubert@icmpe.cnrs.fr (J.-M. Joubert).

0022-3115/$ - see front matter © 2010 Elsevier B.V. All rights reserved.
doi:10.1016/j.jnucmat.2010.05.002

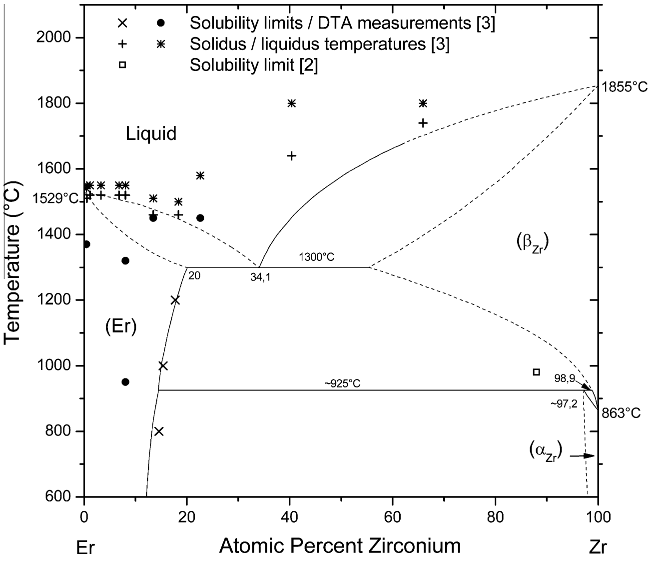

Fig. 1. Er–Zr phase diagram redrawn from Ref. [5].

homogeneity. Several samples were heat-treated at different temperatures to reach thermodynamic equilibrium. To protect the samples from oxygen contamination, they were sealed in silica tubes under high vacuum (10^{-6} mbar) or partial argon atmosphere (Arcal 1 grade, 200 mbar) for the samples annealed at 1200 °C, and protected from the silica by a tantalum sheet. The chosen temperatures and annealing times were as follows: 500 °C (4400 h), 850 °C (1000 h), 1000 °C (1000 h), 1100 °C (500 h) and 1200 °C (500 h). After heat treatment, the samples were quenched into cold water. We made sure that the samples had effectively reached equilibrium by a careful study of the microstructure before and after the heat treatment coupled with a verification of the phase homogeneity by electron probe micro analysis (EPMA).

Pieces of each sample were mounted with phenolic hot (170 °C) resin with carbon filler, and then mechanically polished on 600/1200/4000 SiC grinding paper and on cloths with 6 and 3 μm diamond paste. A final polish using a HF – Struers OPS has been used to smooth the surface. Metallographic examination of the microstructure was performed optically and by using a scanning electron microscope (SEM, 6400 JEOL) with a LaB_6 filament. The composition of each phase has been measured by EPMA (SX 100 CAMECA). Each phase has been subjected to approximately 30 measuring points that have been averaged. The associated experimental standard deviation was lower than 1 at.% showing that each phase was homogeneous.

The samples annealed at 500 °C required the use of a scanning transmission electron microscope (STEM, Jeol FEG-STEM 2010). The sample was cut into a 1 mm thick slice, mechanically polished to a 100 μm thickness with SiC papers (320/600/1200). Then, electrolytic polishing was used to reduce the thickness (≈100 nm around the hole) until perforation. The microscope was equipped with an energy dispersive spectroscopy detector allowing the measurement of composition at a very fine level.

X-ray diffraction (XRD) data have been collected at room temperature on a Bruker D8 Advance diffractometer, using slices of the samples, because of their ductile nature. Due to the strong texture of the samples, the data have been refined using the Full Pattern Matching technique (background, cell parameters and full profile fitting with no intensity constraint) as implemented in the Fullprof program [8].

For the thermal analysis measurements, we have used a multi differential scanning calorimeter (DSC, HTC SETARAM). The heating rate was 10 °C/min. For the measurements involving liquidus, we could not use a conventional DTA system because of the reactivity of the melt with the crucibles and of the high vapor pressure of erbium leading to contamination of the apparatus. In order to

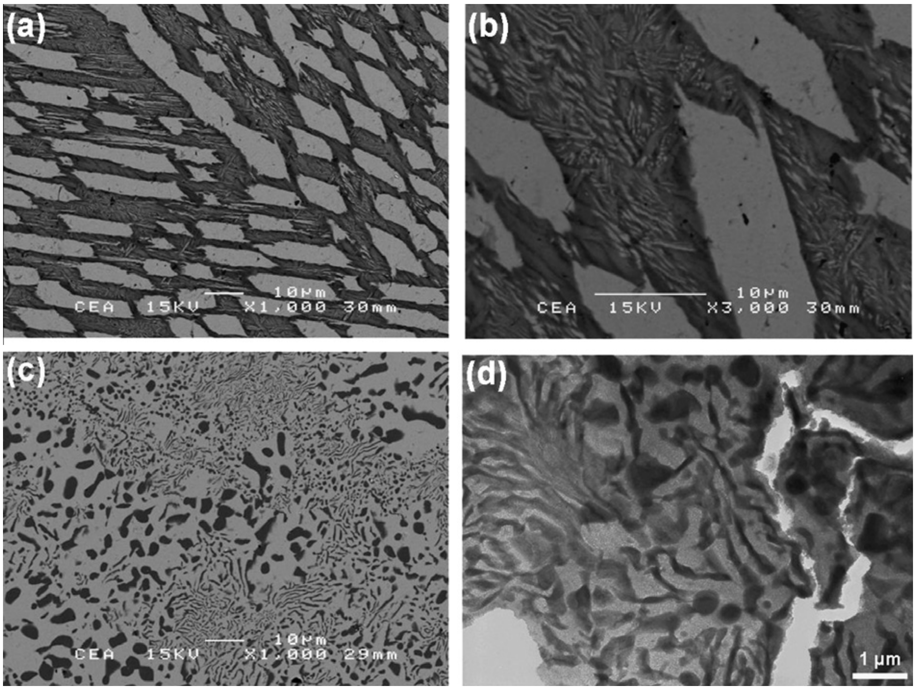

Fig. 2. Back-scattered electron SEM micrographs of samples (a and b) $Er_{41.1}Zr_{58.9}$ heat-treated at 1200 °C, (c) $Er_{61.6}Zr_{38.4}$ heat-treated at 850 °C and (d) bright field TEM picture of $Er_{66}Zr_{34}$ heat-treated at 500 °C. In each image, the erbium solid solution appears as the brightest phase.

obtain the liquidus and solidus temperatures, we used Simple Thermal Analysis (STA). The sample temperature was recorded using a Minolta/Land Cyclops 152A pyrometer during progressive heating or cooling runs at various rates in an induction furnace under argon atmosphere. The incipient melting was generally detected visually, while the complete melting was generally detected by the fact that, in spite of increasing the power, the sample temperature remained constant. The experiment was calibrated by measuring the melting point of pure zirconium and was shown to be accurate to within ±40 °C.

3.2. Results

Examples of the microstructure observed for two-phase samples annealed at different temperatures are shown in Fig. 2. On the SEM images, the solid solution based on pure zirconium (Zr) appears darker than the one based on pure erbium (Er). The micrograph of the sample $Er_{41.1}Zr_{58.9}$ heat-treated at 1200 °C (Fig. 2a) shows a typical Widmanstätten microstructure (Fig. 2b) with re-precipitated erbium in the zirconium matrix, due to solute rejection, characteristic of $(\beta_{Zr}) \rightarrow (\alpha_{Zr})$ transformation. In Fig. 2c is shown the microstructure of a sample of composition $Er_{61.6}Zr_{38.4}$, heat-treated at 850 °C. The microstructure is finer than the one obtained after higher temperature heat treatment. The microstructure of the samples heat-treated at 500 °C was even finer and could neither be visualized by SEM nor analyzed by EPMA. Therefore, we analyzed these samples by STEM (bright field), as shown in Fig. 2d. Due to a preferential erosion of the rare earth during the preparation yielding a lower thickness of (Er) phase, the erbium solid solution appears brighter than (α_{Zr}) phase. The erbium solubility limit in (α_{Zr}) was obtained from the sample $Er_{42}Zr_{58}$ while Zr solubility in (Er) was measured from the sample $Er_{66}Zr_{34}$.

The different phases present in the samples heat-treated at 850 °C, 1000 °C, 1100 °C and 1200 °C, have been analyzed by EPMA in order to determine their chemical composition and by XRD for lattice parameter determination (Table 1).

For each temperature, two samples of different compositions have been synthesized. As can be inferred from Table 1, no significant differences are observed between the analyses of the two constituting phases in both samples. This is an additional confirmation that the samples are close to thermodynamic equilibrium. In the XRD patterns, we could only observe reflections corresponding to *hcp* phases, even for the samples annealed at the highest temperatures, indicating, that the *bcc* (β_{Zr}) phase could not be retained at room temperature and has retransformed into *hcp* (α_{Zr}) during quenching in agreement with the microstructure observations. Therefore, every sample contains two *hcp* phases corresponding to (Er) and (Zr) solid solutions that could only be distinguished by comparing their lattice parameters. Both *a* and *c* cell parameters of most samples linearly decrease as a function of Zr composition (Fig. 3a and b). This is in agreement with the difference between the atomic radii of Er (1.78 Å) and Zr (1.60 Å). However, the lattice parameters of the Zr-rich phase of the sample heat-treated at 1200 °C are very different from what could be expected from its measured composition. The contraction observed can be attributed to the strains generated by the $(\beta_{Zr}) \rightarrow (\alpha_{Zr})$ transformation during quenching and/or to solute rejection. Solute rejection is responsible for lattice contraction because of the larger atomic radius of Er compared to Zr.

We have measured the peritectoid temperature by DSC using samples of composition $Er_{40}Zr_{60}$ (Fig. 4) and $Er_{25}Zr_{75}$. The measured temperature during heating is 1045 ± 20 °C. The solidus and liquidus temperatures have been investigated by STA. The obtained temperatures are listed in Table 2. In one occasion, the STA measured temperatures have been confirmed by a DTA measure-

Table 1
Phase compositions (determined by EPMA) and lattice parameters (determined by XRD) of the different heat-treated samples.

	Equilibrium temperature (°C)	Phase	Composition (at.%)	Lattice parameters *a* (Å)	(±0.0005 Å) *c* (Å)
$Er_{42}Zr_{58}$	500	(Zr)	$Er_{12.3}Zr_{87.7}$		
		(Er)	$Er_{85.5}Zr_{14.5}$		
$Er_{66}Zr_{34}$	500	(Zr)	$Er_{12.4}Zr_{87.6}$		
		(Er)	$Er_{92.5}Zr_{7.5}$		
$Er_{34.9}Zr_{65.1}$	850	(Zr)	$Er_{14.9}Zr_{85.1}$	3.2786	5.1882
		(Er)	$Er_{88.7}Zr_{11.3}$	3.5222	5.5305
$Er_{61.6}Zr_{38.4}$	850	(Zr)	$Er_{15.4}Zr_{84.6}$		
		(Er)	$Er_{87.9}Zr_{12.1}$		
$Er_{40.5}Zr_{59.5}$	1000	(Zr)	$Er_{26.0}Zr_{74.0}$		
		(Er)	$Er_{79.0}Zr_{21.0}$		
$Er_{36.0}Zr_{64.0}$	1000	(Zr)	$Er_{25.3}Zr_{74.7}$	3.3041	5.2156
		(Er)	$Er_{79.8}Zr_{20.2}$	3.4889	5.4774
$Er_{30}Zr_{70}$	1050	(Zr)	$Er_{33.0}Zr_{67.0}$		
		(Er)	$Er_{75.6}Zr_{24.4}$		
$Er_{41.0}Zr_{59.0}$	1100	(Zr)	$Er_{21.0}Zr_{79.0}$		
		(Er)	$Er_{71.9}Zr_{28.1}$		
$Er_{66.3}Zr_{33.7}$	1100	(Zr)	$Er_{21.8}Zr_{78.2}$	3.2888	5.2385
		(Er)	$Er_{67.9}Zr_{32.1}$	3.4507	5.4177
$Er_{41.1}Zr_{58.9}$	1200	(Zr)	$Er_{34.6}Zr_{65.4}$	3.2892	5.1950
		(Er)	$Er_{68.3}Zr_{31.7}$	3.4470	5.4247
$Er_{66.7}Zr_{33.3}$	1200	(Zr)	$Er_{33.5}Zr_{66.5}$		
		(Er)	$Er_{69.3}Zr_{30.7}$		

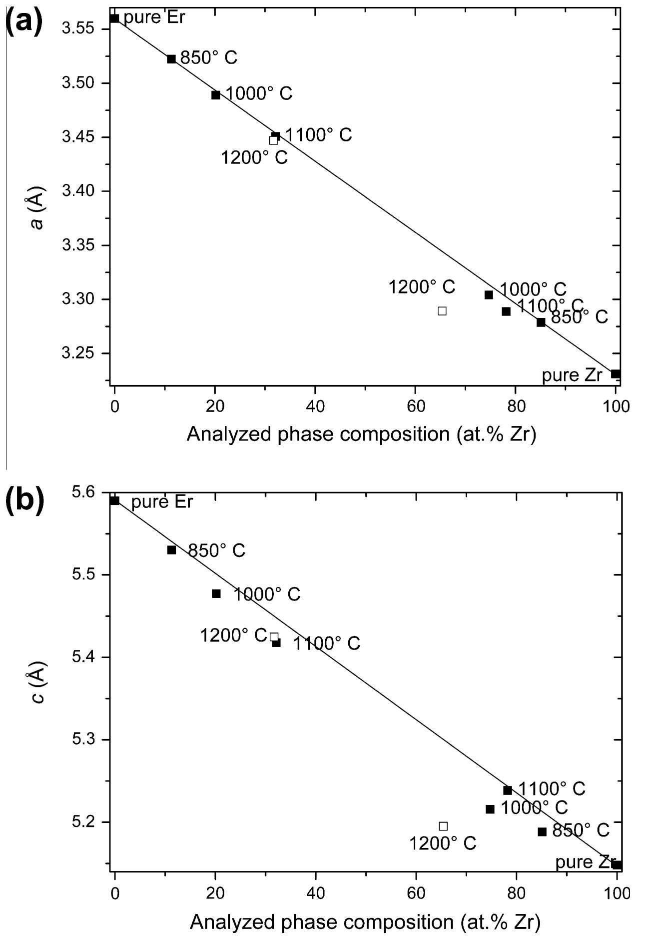

Fig. 3. Lattice parameters (a) *a* and (b) *c* of the *hcp* phase as a function of zirconium composition in the samples heat-treated at 850 °C, 1000 °C, 1100 °C and 1200 °C.

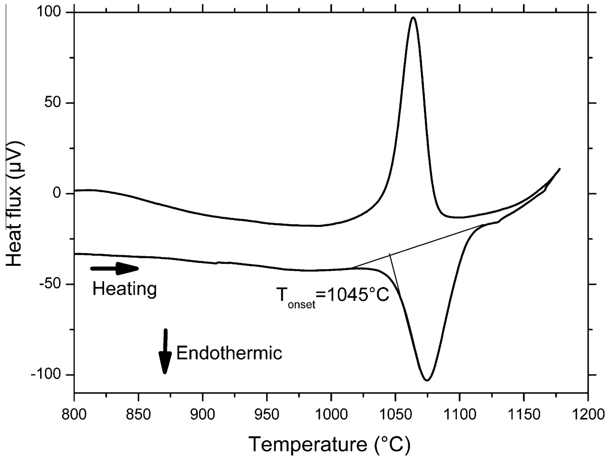

Fig. 4. DSC signal of a sample of composition $Er_{40}Zr_{60}$ (the baseline has been subtracted).

Table 2
Thermal analysis results. The temperatures corresponding to the different events are indicated in °C.

Sample	Liquidus	Solidus	Peritectoid	Allotropic or solvus	Technique
Zr	1840			905	STA
$Er_{10}Zr_{90}$				975	DSC
$Er_{20}Zr_{80}$		1550		950	STA
$Er_{25}Zr_{75}$			1045	1010	DSC
$Er_{35}Zr_{65}$	1480	1450	1050		STA
$Er_{40}Zr_{60}$			1045		DSC
$Er_{45}Zr_{55}$	1430	1400			STA
$Er_{52}Zr_{48}$	1406	1385			STA
$Er_{60}Zr_{40}$	1390	1375			STA
$Er_{66.5}Zr_{33.5}$	1415	1405			DTA
$Er_{68}Zr_{32}$	1415	1390			STA
$Er_{80}Zr_{20}$	1450	1420			STA
$Er_{90}Zr_{10}$	1490	1460			STA

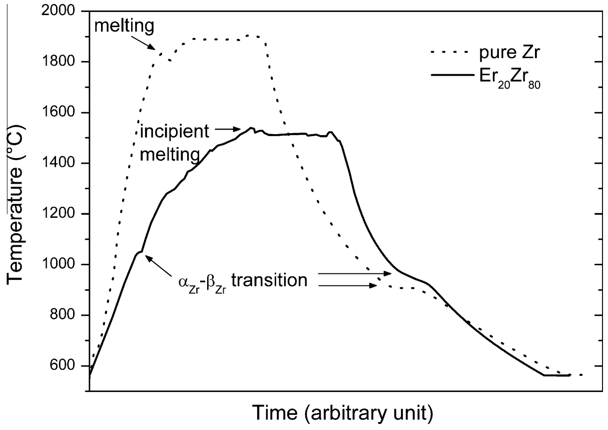

Fig. 5. Simple Thermal Analysis curves of pure Zr and $Er_{20}Zr_{80}$ (heating and cooling).

ment. As an example, Fig. 5 presents two curves obtained by this technique on pure Zr and $Er_{20}Zr_{80}$, respectively. Pure Zr was considered as a calibration sample, and allowed an evaluation of the error on the temperature measurement. Both curves present inflections related to the (α_{Zr})–(β_{Zr}) transformation indicating that even solid state transformations can be detected by this technique. For $Er_{20}Zr_{80}$, as for most studied samples, it is quite difficult to distinguish liquidus and solidus temperatures, which is an indication that they are very close.

As-cast samples were systematically observed by metallography in order to estimate the eutectic composition. Samples with compositions ranging from 30 at.% Zr to 70 at.% Zr have been synthesized by steps of 5 at.% Zr (see Fig. 6). The observation of the eutectic microstructure in the samples $Er_{55}Zr_{45}$ and $Er_{50}Zr_{50}$ allows to locate the eutectic point at the approximate composition 45–50 at.% Zr.

The proposed phase diagram, obtained from the measurements described above, is shown in Fig. 7.

4. Thermodynamic modeling

The system was assessed with the CALPHAD method [9]. This technique consists in describing the Gibbs energies of all the phases present in the system as a function of temperature and composition.

4.1. Pure elements

The Gibbs energies of the pure elements are defined with respect to their stable states at 298.15 K and 10^5 Pa (*hcp* for Er, *hcp* for Zr). The Gibbs energies used for the pure elements in both structures and in liquid state are those proposed by the Scientific Group Thermodata Europe database (SGTE) [10].

4.2. Solution phases

Liquid, *hcp* and *bcc* phases were modeled using the substitutional solution model. The Gibbs energy of each phase φ (G^φ) is described as a function of the molar fraction of the elements x_{Er} and x_{Zr} as the sum of three terms: reference (${}^{ref}G^\varphi$), ideal (${}^{id}G^\varphi$), and excess (${}^{ex}G^\varphi$).

$$G^\varphi = {}^{ref}G^\varphi + {}^{id}G^\varphi + {}^{ex}G^\varphi \quad (1)$$

where:

$${}^{ref}G^\varphi = x_{Er}G^\varphi_{Er} + x_{Zr}G^\varphi_{Zr} \quad (2)$$

$${}^{id}G^\varphi = RT(x_{Er}\ln x_{Er} + x_{Zr}\ln x_{Zr}) \quad (3)$$

$${}^{ex}G^\varphi = x_{Er}x_{Zr}\sum_{\nu=0}^{n} {}^{\nu}L^\varphi_{Er,Zr}(x_{Er} - x_{Zr})^\nu \quad (4)$$

The models are consistent with the zirconium alloys database [11]. The excess parameters ($L^\varphi_{Er,Zr}$) have been evaluated using the experimental data and can be, or not, temperature dependent. The *hcp* phase has been modeled with a miscibility gap in order to take into account the (Er) and (α_{Zr}) phase separation.

4.3. Results

The optimization has been carried out using the Parrot module of the Thermo-Calc software [12]. All the experimental data obtained in the present work have been used to assess the system with uncertainties and weights chosen in order to reach a satisfactory agreement with all the data. Due to the uncertainties of the literature data, none of them have been used. The starting values for the parameters have been taken from the assessment of the Gd–Zr system by Zinkevich et al. [13]. The obtained final parameters are given in Table 3 after rounding to the last significant digit. The phase diagram, calculated with these parameters, is shown in

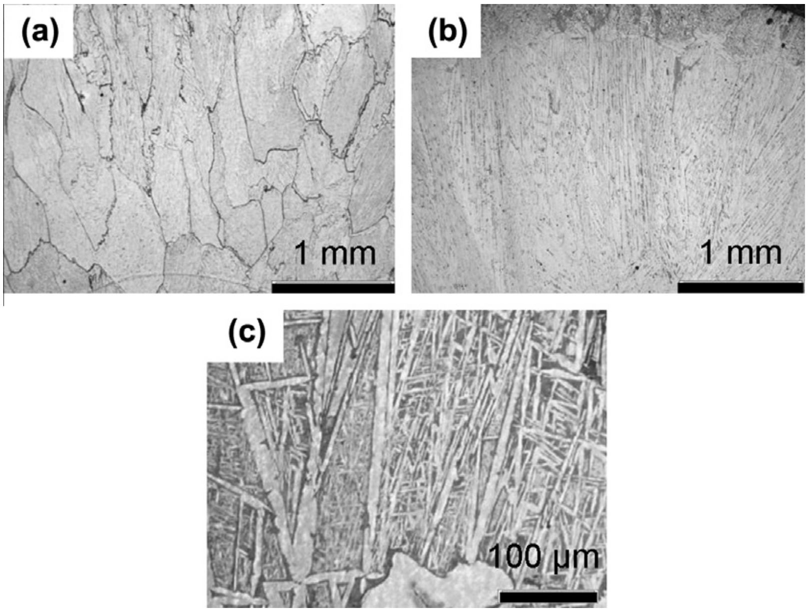

Fig. 6. Typical microstructures obtained on different as-cast samples observed by optical metallography showing (a) primary Er-crystals (sample $Er_{60}Zr_{40}$), (b) eutectic microstructure (sample $Er_{55}Zr_{45}$) and (c) primary Zr-crystals (sample $Er_{40}Zr_{60}$).

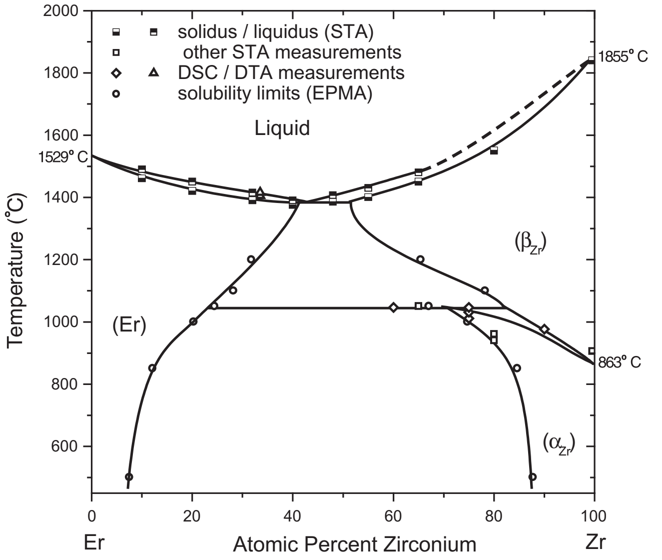

Fig. 7. Experimental results of the present investigation and proposed Er–Zr phase diagram.

Table 3
List of optimized parameters (J mol^{-1}).

Phase	Parameter
Liquid	${}^{0}L^{\text{liq}}_{\text{Er,Zr}} = 14,200$
	${}^{1}L^{\text{liq}}_{\text{Er,Zr}} = 2650$
bcc	${}^{0}L^{bcc}_{\text{Er,Zr}} = 15,742 + 5.1T$
	${}^{1}L^{bcc}_{\text{Er,Zr}} = 281$
hcp	${}^{0}L^{hcp}_{\text{Er,Zr}} = 21,150 + 1.5T$
	${}^{1}L^{hcp}_{\text{Er,Zr}} = 9060 - 5.5T$

Fig. 8. A comparison between experimental and calculated invariant temperatures is given in Table 4.

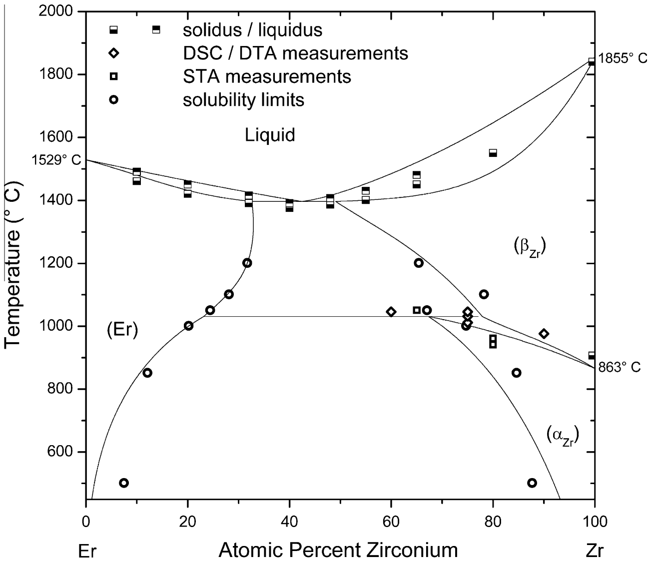

Fig. 8. Experimental results of the present investigation and calculated Er–Zr phase diagram.

Table 4
Invariant reactions with corresponding experimental and calculated temperatures.

Invariant reaction	$T_{\text{exp.}}$ (°C)	$T_{\text{calc.}}$ (°C)
Liquid → (Er) + (β_{Zr})	1380	1397
(Er) + (β_{Zr}) → (α_{Zr})	1045	1031

5. Discussion

5.1. Experimental determination of the phase diagram

The solubility of erbium in hexagonal zirconium increases drastically (up to approximately 30 at.% Er) as a function of temperature up to 1000 °C. The sudden decrease between 1000 °C and 1100 °C is in good agreement with the DSC measurement of the peritectoid transformation temperature (1045 °C). The given transition and the solubility limits are also in excellent agreement with a DSC run on a sample of composition $Er_{25}Zr_{75}$ (see Fig. 7 and Table 2).

The solubilities of Er in (β_{Zr}) and of Zr in (Er) reach 40 at.% at the eutectic temperature. The large homogeneity domain of these two solid solutions is in good agreement with the small composition range in which eutectic microstructure has been evidenced. The eutectic temperature has been determined by means of STA (1380 °C).

The STA technique we have used has allowed investigating both liquidus and solidus temperatures. For every sample, these temperatures were very close. The proposed diagram is in profound disagreement with the one drawn in Ref. [5] based on the few experimental data described in Section 2. The discrepancies may be attributed to the low purity of the materials used, the possible oxygen contamination and the absence of phase composition analysis.

5.2. Assessed phase diagram

The optimized phase diagram reproduces well the experimental results, except for the calculated low temperature solid solubilities which are found to be smaller than the experimental values. We purposely did not add parameters to force the low temperature solubilities in order to keep the model as simple as possible and because we cannot exclude that the samples annealed at 500 °C had not reached equilibrium. The calculated peritectoid temperature is very close to the experimental one. The eutectic reaction occurs 17 °C above the experimental one which is in the range of the experimental error.

6. Conclusion

We have re-determined and modeled the erbium–zirconium phase diagram. Several experimental techniques (several thermal analysis techniques, EPMA, TEM, XRD) have been used to investigate the phase equilibria and phase transformations. The obtained results lead to a new version of the phase diagram very different from the one available in the literature. It is mainly characterized by large terminal solubilities on both sides, unusual for Zr-rare earths systems. The erbium–zirconium system has been assessed using the Calphad approach. The experimental and calculated diagrams are in good agreement.

Acknowledgement

The authors want to thank Didier Hamon who provided expert help for the EPMA.

References

[1] J.-C. Brachet, P. Olier, S. Urvoy, V. Vandenberghe, C. Chabert, Addition of erbium as a neutronic burnable poison in zirconium base nuclear fuel cladding tube, in: Proc. of the TopFuel 2009 Conf., Paris, Paper 2189, 2009.
[2] C. Armantrout, Quarterly Metallurgical Progress Report No. 3, US Dept. of the Interior, Bu. of Mines, Albany Metallurgy Research Center, 1959.
[3] B. Love, Wright Air Development Division Technical Report 60-74. The metallurgy of Yttrium and the rare earth metals. Part I. Phase relationships, Universitätsbibliothek Hannover und Technische Informationsbibliothek, Hannover, 1960.
[4] M. Copeland, H. Kato, Rare-earth-rich alloys, in: Proc. of the Symposium on Physics and Material Problems of Reactor Control Rods, Vienna, 1963, pp. 295–317.
[5] C.B. Alcock, K.T. Jacob, S. Zador, O. Kubaschewski-von Goldbeck, H. Nowotny, K. Seifert, O. Kubaschewski, Atom. Energy Rev. 6 (1976) 1–268 (special issue).
[6] H. Okamoto, Phase Diagrams for Binary Alloys, Desk Handbook, ASM International, 2000.
[7] P. Villars, Pauling File Binary Edition, Version 1.0, 2002.
[8] J. Rodríguez-Carvajal, Commission on Powder Diffraction, Newsletter 26 (2001) 12–19.
[9] H.L. Lukas, S.G. Fries, B. Sundman, Computational Thermodynamics, the Calphad Method, Cambridge University Press, Cambridge, New York, Melbourne, Madrid, Cape Town, Singapore, São Paulo, 2007.
[10] A.T. Dinsdale, Calphad 15 (4) (1991) 317–425.
[11] N. Dupin, I. Ansara, C. Servant, C. Toffolon, C. Lemaignan, J.-C. Brachet, J. Nucl. Mater. 275 (1999) 287–295.
[12] B. Sundman, B. Jansson, J.O. Andersson, Calphad 9 (2) (1985) 153–190.
[13] M. Zinkevich, N. Mattern, H.J. Seifert, J. Phase Equilib. 22 (1) (2001) 43–50.